Physics in Medicine & Biology

IPEM
Institute of Physics and
Engineering in Medicine

PAPER • OPEN ACCESS

Dual energy CT for a small animal radiation research platform using an empirical dual energy calibration

To cite this article: Manuela Anna Duda *et al* 2022 *Phys. Med. Biol.* **67** 135009

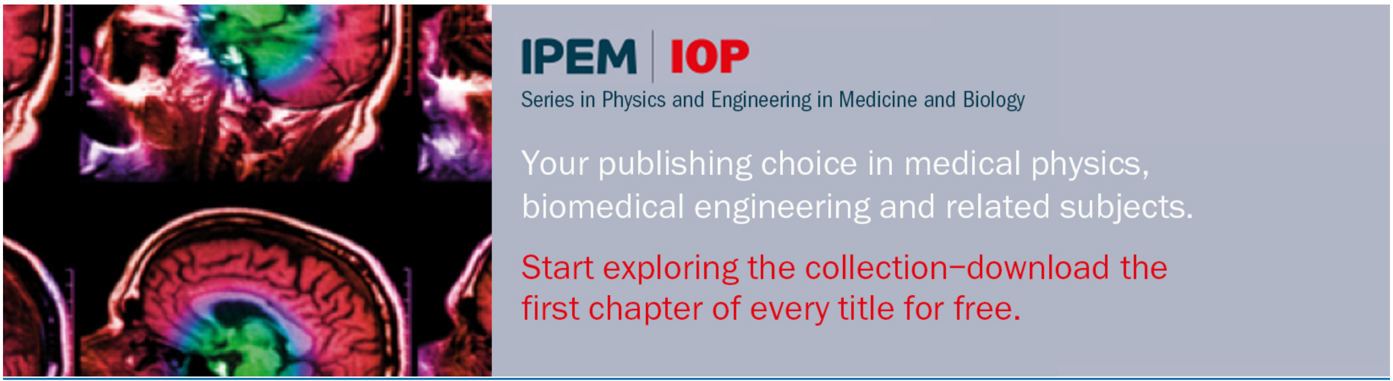

IOP Publishing Phys. Med. Biol. 67 (2022) 135009 https://doi.org/10.1088/1361-6560/ac7770

Physics in Medicine & Biology

IPEM
Institute of Physics and Engineering in Medicine

CrossMark

OPEN ACCESS

RECEIVED
11 January 2022

REVISED
1 June 2022

ACCEPTED FOR PUBLICATION
9 June 2022

PUBLISHED
29 June 2022

PAPER

Dual energy CT for a small animal radiation research platform using an empirical dual energy calibration

Manuela Anna Duda[1,2,*], **Andreas Grad**[1,2], **Severin Kampfer**[1,2], **Sophie Dobiasch**[1,3], **Stephanie Elisabeth Combs**[1,3,4] **and Jan Jakob Wilkens**[1,2]

[1] Department of Radiation Oncology, School of Medicine and Klinikum rechts der Isar, Technical University of Munich (TUM), Munich, Germany
[2] Physics Department, Technical University of Munich (TUM), Garching, Germany
[3] Institute of Radiation Medicine (IRM), Department of Radiation Sciences (DRS), Helmholtz Zentrum München, Neuherberg, Germany
[4] German Cancer Consortium (DKTK), Munich, Germany
[*] Author to whom any correspondence should be addressed.

E-mail: manuela.duda@tum.de

Keywords: small animal, computed tomography, SARRP, CT, dual energy, spectral, imaging

Abstract

Objective. Dual energy computed tomography (DECT) has been shown to provide additional image information compared to conventional CT and has been used in clinical routine for several years. The objective of this work is to present a DECT implementation for a Small Animal Radiation Research Platform (SARRP) and to verify it with a quantitative analysis of a material phantom and a qualitative analysis with an *ex-vivo* mouse measurement. *Approach.* For dual energy imaging, two different spectra are required, but commercial small animal irradiators are usually not optimized for DECT. We present a method that enables dual energy imaging on a SARRP with sequential scanning and an Empirical Dual Energy Calibration (EDEC). EDEC does not require the exact knowledge of spectra and attenuation coefficients; instead, it is based on a calibration. Due to the SARRP geometry and reconstruction algorithm, the calibration is done using an artificial CT image based on measured values. The calibration yields coefficients to convert the measured images into material decomposed images. *Main results.* To analyze the method quantitatively, the electron density and the effective atomic number of a material phantom were calculated and compared with theoretical values. The electron density showed a maximum deviation from the theoretical values of less than 5% and the atomic number of slightly more than 6%. For use in mice, DECT is particularly useful in distinguishing iodine contrast agent from bone. A material decomposition of an *ex-vivo* mouse with iodine contrast agent was material decomposed to show that bone and iodine can be distinguished and iodine-corrected images can be calculated. *Significance.* DECT is capable of calculating electron density images and effective atomic number images, which are appropriate parameters for quantitative analysis. Furthermore, virtual monochromatic images can be obtained for a better differentiation of materials, especially bone and iodine contrast agent.

1. Introduction

Dual energy imaging offers several advantages over conventional single energy CT (SECT) imaging. For instance, material decomposed images and virtual monoenergetic images can be calculated. In addition, dual energy imaging provides structural information such as electron density or effective atomic number. Through these dual energy images, a better differentiation of materials can be achieved and quantitative measurements can be performed. Preclinical cancer research involving high-precision irradiation of mice is very common, but nevertheless, research devices and clinical devices are still very different. For human medicine, different dual energy CT devices are already commercially available (Sellerer *et al* 2018). Here, dual energy imaging is used for cardiovascular imaging, abdominal and oncological studies, among others (Agostini *et al* 2019). For preclinical cancer research, dual energy imaging is also very useful, but so far, there are no dedicated commercially available dual energy imaging devices for image-guided irradiation of mice. However, it could be shown that quantitative DECT imaging is feasible for small animal irradiators with an integrated cone beam CT (CBCT) system (Schyns *et al* 2016). Other previous work compared the effect of various image reconstruction techniques for DECT (Vaniqui *et al* 2018). Different small animal irradiators have been developed, which combine imaging and radiation treatment (Verhaegen *et al* 2011). One approach was started by the Johns Hopkins University and commercialized by XStrahl Ltd. (Walsall, UK) (Wong *et al* 2008): The SARRP can be used for image-guided irradiations but also for tumor observation and follow-up CTs. For imaging, DECT provides a better contrast between different materials and offers further processed images. The mouse treatment procedure is similar to that for humans, but the mouse is under anesthesia and so imaging, treatment planning and irradiation usually take place in one session (Dobiasch *et al* 2017). To avoid frequent anesthesia, fewer fractions are generally scheduled with higher treatment doses. As the proportions of mice and humans differ a lot, the radiation treatment is performed with kV photon beams rather than MV photon beams (Verhaegen *et al* 2011). For dose calculation, the SARRP treatment planning system assigns one of five materials (air, lung, muscle, fat, bone) to each voxel in the CT image. This segmentation is crucial for a proper dose calculation (Bazalova-Carter *et al* 2008). As soft tissue contrast on CT is very low, contrast agent is administered in many cases. This can mistakenly lead to segmentation as bone for contrast-enhanced tissue. Dual energy imaging could solve this problem by providing corrected imaging values and so a correct segmentation for dose calculation (Vaniqui *et al* 2017).

2. Materials and methods

2.1. General dual energy imaging

Dual energy imaging for clinical CT applications has already been developed by Alvarez and Macovski in the late 1970s (Alvarez and Macovski 1976). They presented a technique for obtaining complete energy dependent information in a CT system. The attenuation coefficient, which depends on both the material and the energy, is used to obtain this information. For any material without a K-edge in the respective energy range, the attenuation coefficient $\mu(x, y, E)$ at an energy E in a voxel (x, y) can be expressed as a linear combination of the attenuation coefficients $\mu_{1,2}$ of two basis materials 1 and 2:

$$\mu(x, y, E) = a_1(x, y) \cdot \mu_1(E) + a_2(x, y) \cdot \mu_2(E). \tag{1}$$

The scalar factors $a_{1,2}$ represent basis material images, which denote the volume fraction of the basis materials contributing to the total attenuation coefficient of the measured object. The intent of dual energy imaging is to obtain these basis material images $a_{1,2}$. As in x-ray systems line integrals of the attenuation coefficient along the beam path $\vec{s}$ are measured, equation (1) is expressed with the corresponding line integrals (Alvarez and Macovski 1976):

$$\int \mu(x, y, E)\mathrm{d}s = p_1 \cdot \mu_1(E) + p_2 \cdot \mu_2(E), \tag{2}$$

where

$$p_1 = \int a_1(x, y)\mathrm{d}s \quad \text{and} \quad p_2 = \int a_2(x, y)\mathrm{d}s. \tag{3}$$

Accordingly to the basis material images $a_{1,2}$, the line integrals $p_{1,2}$ are called basis material projections. In order to get the line integrals $p_{1,2}$, there must be two independent measurements with two different spectra (Alvarez and Macovski 1976). The calculation of the basis material images $a_{1,2}$ from the two measured attenuation data is called material decomposition. Many material decomposition algorithms require precise knowledge of either the x-ray spectrum or the attenuation coefficient to calculate the basis material images. An approach without these requirements is performing a calibration with polynomial functions (Cardinal and Fenster 1990, Kappadath and Shaw 2003). In particular, we use a method called EDEC from Stenner *et al* (Stenner *et al* 2007). The material decomposition converts the two polychromatic projections q_{low} (acquired with the low energy spectrum) and q_{high} (acquired with the high energy spectrum) into basis material projections $p_{1,2}$:

$$p_{1,2} = \vec{c}_{1,2} \cdot \vec{b}(q_{\text{low}}, q_{\text{high}}), \tag{4}$$

where $\vec{c}_{1,2}$ are coefficient vectors and $\vec{b}$ are basis functions. The reconstruction of $p_{1,2}$ yields the basis material images $a_{1,2}$ of equation (1):

$$a_{1,2} = R^{-1}p_{1,2} = R^{-1}(\vec{c}_{1,2} \cdot \vec{b}(q_{\text{low}}, q_{\text{high}})) = \vec{c}_{1,2} \cdot R^{-1}\vec{b}(q_{\text{low}}, q_{\text{high}}), \tag{5}$$

where R^{-1} is the inverse Radon transform. The coefficient vectors $\vec{c}_{1,2}$ allow the conversion from the polychromatic raw data into the material decomposed data. The purpose of EDEC is therefore the determination of $\vec{c}_{1,2}$. For our application, we used the EDEC method as a basis and adapted it for our setup.

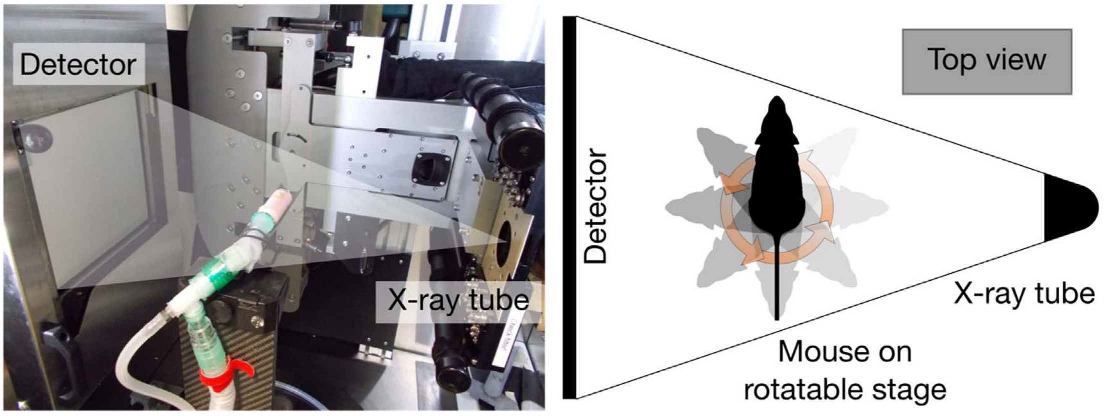

Figure 1. SARRP in imaging mode. The x-ray tube and the detector are in a fixed position, the mouse is placed in the prone position on a mouse bed. In CT imaging, the mouse is rotated horizontally, i.e. the x-ray beam passes through the entire length of the mouse from some angles and through the short axis from other angles.

2.2. Experimental setup

The dual energy measurements were performed at a Small Animal Radiation Research Platform (SARRP, Xstrahl Ltd., Walsall, UK), which is used for preclinical cancer research in mice. The SARRP can acquire CBCT images, plan and perform radiation treatment. It is equipped with an x-ray tube, a flat panel detector, a rotatable stage and filter equipment.

The x-ray tube with a tungsten anode has two focal spots. For imaging the fine focus with a focal spot size of $d = 1.0$ mm and a maximum target power of 640 W is used. The flat panel detector XRD 0822 (PerkinElmer Inc., Massachusetts) provides 1024×1024 pixels with a native pixel size of 0.2 mm. With a magnification of about 1.8 and the finest reconstruction protocol, an effective pixel size of 0.11 mm can be achieved. The rotatable stage is used to mount a mouse bed or sample table. In contrast to clinical systems, the mouse or sample is rotated instead of source and detector (figure 1). The axis of rotation is the sagittal axis of the mouse instead of the longitudinal axis. This means that during a CT acquisition the x-ray beam passes the mouse through both the short and long axis. By default, a 1 mm aluminum (Al) filter for imaging is available.

Our standard single energy CT (SECT) images of mice at the SARRP are acquired at 60 kV with 0.8 mA and with the 1 mm Al filter. For dual energy imaging, two well separated x-ray spectra are necessary. A tube voltage of 50 kV for the low energy spectrum and a tube voltage of 100 kV for the high energy spectrum is used, both filtered with 1 mm Al (figure 2). The tube current is chosen according to the number of projections and the kind of measurement (materials/*ex-vivo*/*in-vivo*). For the measurements on mice, the tube currents are chosen so that the total dose of the two DECT data sets does not exceed the dose of SECT, but the same or a higher image quality is achieved. In addition, the DECT images contain more information than SECT images.

2.3. Dual energy calibration

2.3.1. Calibration phantom

The aim of the dual energy calibration is to obtain the coefficient vectors $\vec{c}_{1,2}$ from equation (4). Therefore, a calibration phantom with well known basis materials is needed. Two characteristics of the calibration phantom must be well considered for the calibration on the SARRP: the materials of the phantom and the geometry with its dimensions. Since dual energy imaging in our facility is intended for treatment planning in mice, basis materials with attenuation properties comparable to those in mice are used. For this purpose, polyoxymethylene (POM) and polyvenylchloride (PVC) are suitable, as these materials behave very similar to soft tissue and bone. We perform the dual energy calibration with two cylinders made of the two basis materials POM (index 1) and PVC (index 2). The cylinder diameters have to be chosen carefully with respect to the imaging task. On the one hand, the cylinders should cover all possible path lengths which can occur in the measured sample. For mouse measurements at SARRP, the longest path length is defined by the length of the mouse. The cylinder diameter is therefore determined by the composition of the mouse along the longitudinal axis. Approximately, this would result in 8 cm soft tissue (replaced with POM) and 2 cm bone (replaced with PVC). On the other hand, the cylinders should be small to avoid beam hardening artifacts. For a calibration phantom with 8 cm POM and 2 cm PVC, hardly any photons reach the detector behind the thickest parts. Since the shape of a mouse approximates an elongated ellipse instead of a circle, the case where only a few photons hit the detector occurs only from a few angles for a mouse. With thick, round samples such as the calibration cylinders, however, this is the case from all angles, so that the reconstruction does not provide reliable values. To handle this conflict, the

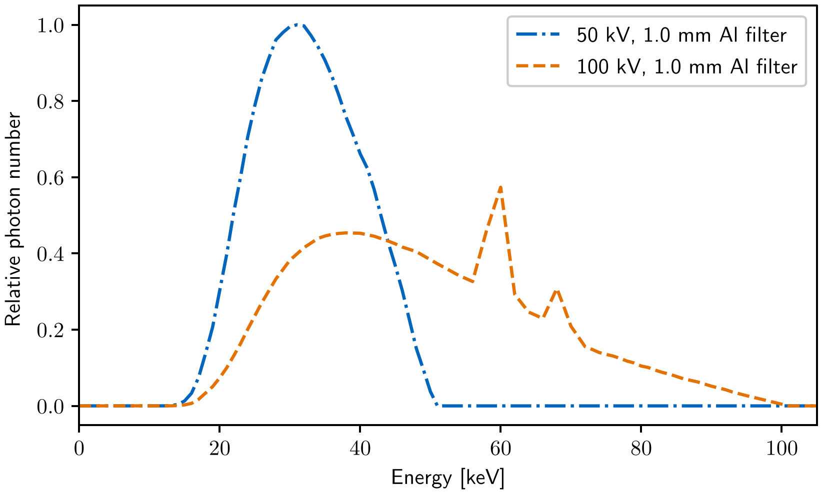

Figure 2. Dual energy spectra. To achieve two well separated spectra, two different tube voltages (50 kV and 100 kV) with the standard 1 mm Al filter are used. The spectra were calculated using the TASMIP algorithm (Boone and Seibert 1997), with the two spectra scaled such that the total photon number is equal.

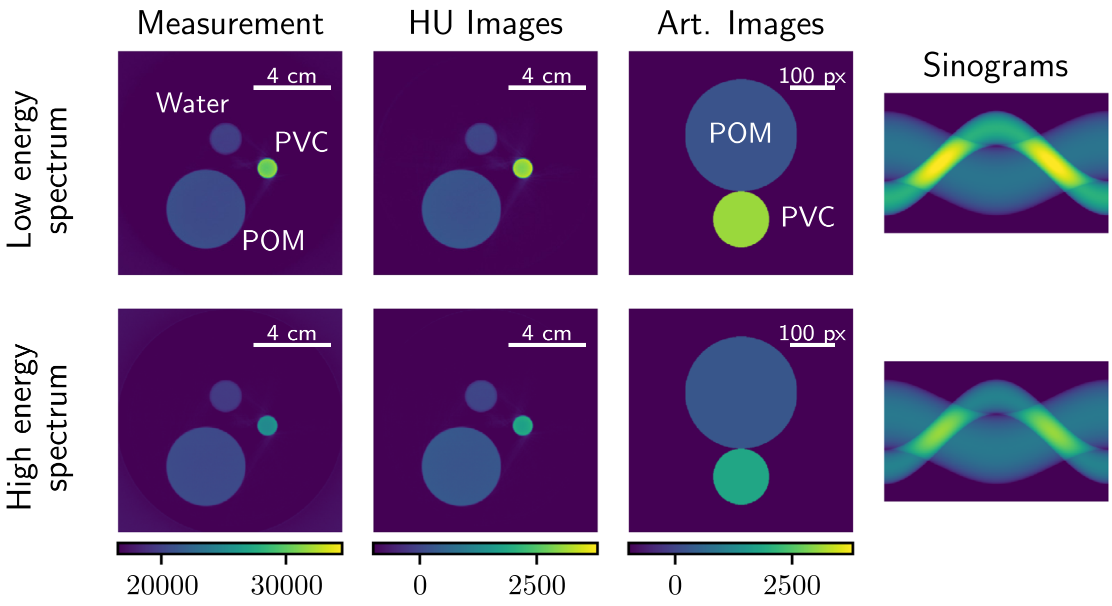

Figure 3. Creation of artificial CT images based on real measurements. Two CT images of the calibration phantom and a water-filled tube are acquired with the low and the high energy spectra. They are converted into Hounsfield units and the mean values of both basis materials are put into an artificial CT image. With a Radon transformation, sinograms of the artificial CT images are obtained.

real calibration measurement is combined with an artificially created image, where the diameters can be varied as needed. For the calibration measurement, a POM cylinder with a diameter of 4 cm and a PVC cylinder with a diameter of 1 cm were chosen. These two dimensions refer to the mean dimensions of soft-tissue and bone in the mouse projections.

2.3.2. Calibration measurement and creation of artificial CT images

The two cylinders and a water-filled tube are placed side by side and a CT is acquired with each of the two spectra (figure 3 ‘Measurement’). The water-filled tube is necessary, because the SARRP scales the CT values v in the range of 0 to $2^{15} - 1$, causing that the same material has different values in different measurements. Therefore, the obtained CT images are first converted to Hounsfield units (HU) (figure 3 ‘HU Images’) using the CT values of the water-filled tube v_{water} and the surrounding air v_{air}:

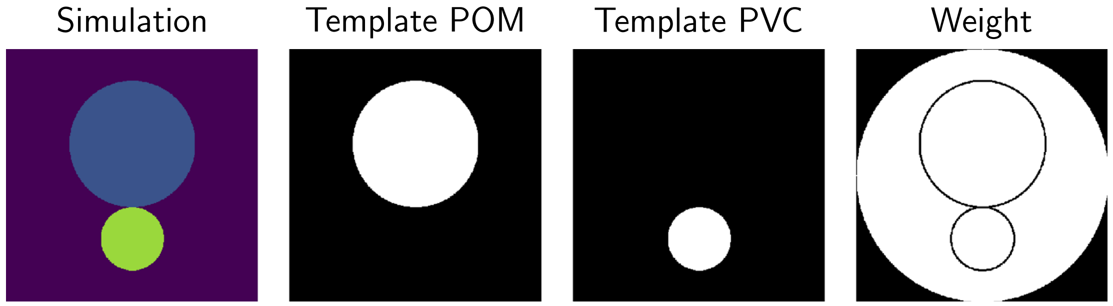

Figure 4. Calibration masks. The template masks define the regions of the basis materials and contain only one basis material. The weight image takes point spread functions into account and indicates whether the content of a pixel is exactly known or not.

$$HU = 1000 \cdot \frac{\nu - \nu_{\text{water}}}{\nu_{\text{water}} - \nu_{\text{air}}}. \tag{6}$$

From the HU images of the measurement, mean values of the basis materials are extracted for both, the low and the high energy data set.

In the next step, two artificial images are created, one for the low and one for the high energy data set. These images shall imitate one slice of a calibration measurement, in which a large POM and a smaller PVC cylinder are placed next to each other. The images therefore contain two circles each, one for POM and one for PVC, which are placed next to each other and whose mean values corresponds to the HU values for the low energy and high energy spectrum, respectively (figure 3 'Art. Images'). Since the values come from the measured CT images of the SARRP, the influences of the spectrum and the detector response are reflected in the artificially generated images. In contrast to the measurement, the diameter of the circles can be freely varied. Since the mouse has much more soft tissue than bone, the POM circle diameter covers about 50% of the image width and PVC covers about 25%. The image size of the artificial images was set to 500 × 500 pixels and originated from the image size of the reconstructions from the SARRP which vary typically between 433 and 465 pixels depending on the reconstruction protocol. With 500 pixels the original image size is slightly exceeded and the calibration can be used for the different protocols.

2.3.3. EDEC with the artificial CT images

Using a Radon transformation R with 801 angles in parallel beam geometry, the artificial images are forward projected into sinograms (q_{low} and q_{high}, figure 3 'Sinograms'). The number of angles is derived from the Nyquist–Shannon theorem, which states that at least 500 px $\cdot\ \pi/2$ angles = 785 angles are needed for a good reconstruction (Kharfi 2012). Of course, it is possible to calibrate with larger image dimensions and more angles, but this requires more computation power and time. The sinograms are then processed into 25 basis sinograms using polynomials:

$$b_n(q_{\text{low}}, q_{\text{high}}) = q_{\text{low}}^k \cdot q_{\text{high}}^l, \tag{7}$$

with $k = 0, \ldots, 4$; $l = 0, \ldots, 4$ and $n = k \cdot 5 + l$ as proposed by Stenner *et al* (Stenner *et al* 2007). The range of the parameters k and l could be varied, but a high number would lead to long computing times and a low number could cause quality loss. A calibration with our parameters takes about three to five minutes.

In the next step, the basis sinograms are backprojected (inverse Radon transform R^{-1} with 801 angles in parallel beam geometry) and one obtains 25 basis images $R^{-1}b_n$. With the prior knowledge about the calibration phantom two masks can be created, namely the template $t_{1,2}(x, y)$ and the weight $w(x, y)$ (figure 4). The template mask is created for each of the two basis materials and has the value 1 for regions with POM or PVC and value 0 everywhere else. As our calibration is done on an artificial CT image, the template is identical with the circle of each material. The weight mask avoids uncertainties due to the point spread functions which occur at the edges of a material. The weight mask has the value 1, whenever it is certain, that a voxel contains only POM, PVC or air. Otherwise, it is zero. A margin of 2 pixels from the edges of the basis materials turned out to be advisable.

The masks and the basis images are used to determine the coefficients $\vec{c}_{1,2}$ of equation (4). Each coefficient vector $\vec{c}_{1,2}$ has a total number of 25 coefficients, which results in total in 50 unknown coefficients. The coefficient vectors $\vec{c}_{1,2}$ can be found by minimizing the least square deviation χ^2 between the linearly combined basis images $\vec{c}_{1,2} \cdot R^{-1}b_n$ and the template images $t_{1,2}(x, y)$. The weight $w(x, y)$ is used to suppress unwanted structures that would affect the optimization (Stenner *et al* 2007):

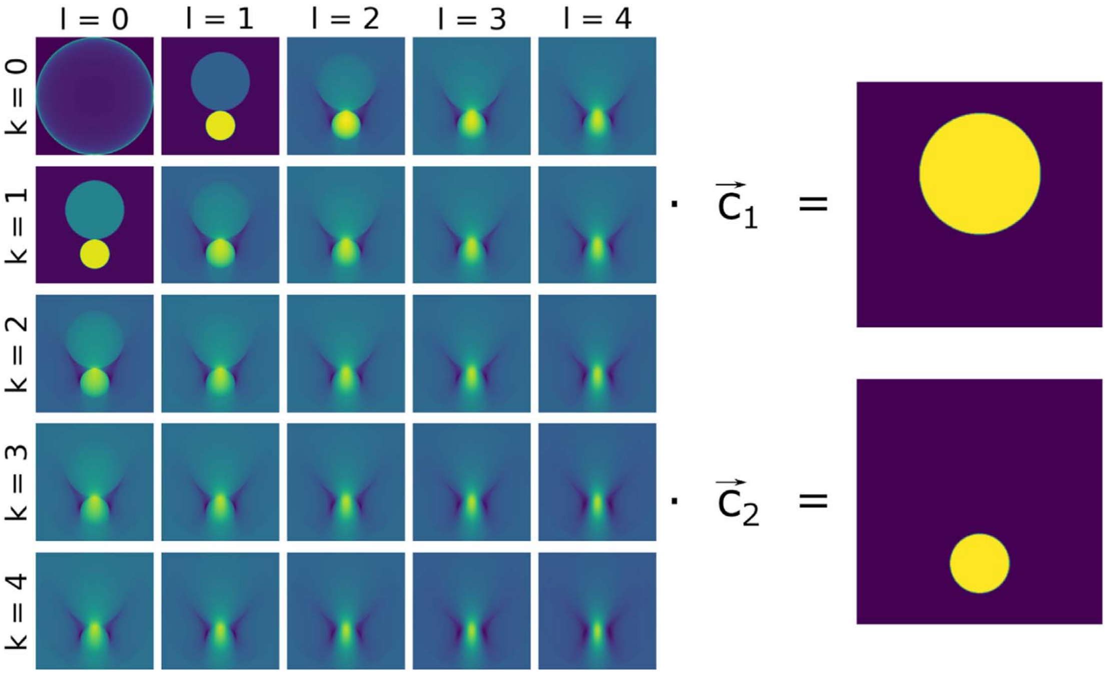

Figure 5. Linearly combined basis images and the template images. The 25 basis images $R^{-1}b_n$ calculated with the coefficients $\vec{c}_{1,2}$ are optimized with a least square deviation to yield the weighted template images $w(x, y) \cdot t_{1,2}(x, y)$.

$$\chi^2 = \int w(x, y) \cdot [\vec{c}_{1,2} \cdot R^{-1}b_n(x, y) - t_{1,2}(x, y)]^2 \, \mathrm{d}x\mathrm{d}y. \tag{8}$$

The optimization process is visually demonstrated in figure 5. The mathematical details are described in the publication of Stenner *et al* (Stenner *et al* 2007).

2.4. Dual energy measurement

Once the calibration is complete and the coefficients are available, the actual dual energy measurements can be processed into material images. The steps are very similar to the calibration: the sample or mouse and a container with water are measured with the same two spectra as in the calibration. Subsequently, the obtained CT raw data are converted into HU and the sinograms q_{low} and q_{high} are calculated. The sinograms are passed through the basis functions (equation (7)) and one obtains 25 basis sinograms b_n. Up to this point, everything is identical to the calibration. Now, instead of reconstructing the 25 basis sinograms, the basis material projections $p_{1,2}$ are directly calculated with the calibration coefficients like in equation (4). Afterwards the two obtained basis material projections are reconstructed into basis material images $a_{1,2}$ (equation (5)). If the measured sample contains POM or PVC, the basis material images can be used for an initial check whether the calibration coefficients and the decomposition of the raw data are correct (expected values for POM and PVC of 1 and 0 in the respective basis material images).

2.5. Further processing methods

Once the material images are available, they can be used for further calculations. For diagnostic purposes, virtual monochromatic images (VMIs) are of great value. For structural information, the material images can also be used to calculate the electron density ρ_{el} and the effective atomic number Z_{eff} (Sellerer *et al* 2019).

2.5.1. Virtual monochromatic images

True monochromatic images are the result of imaging with a monochromatic x-ray beam, typically at a particle accelerator. For polychromatic x-ray beams, as found in the SARRP and in clinical applications, the material images allow the calculation of VMIs at a selectable photon energy E_0 using equation (1):

$$\mu(x, y, E_0) = a_1(x, y) \cdot \mu_1(E_0) + a_2(x, y) \cdot \mu_2(E_0), \tag{9}$$

where $a_{1,2}(x, y)$ are the basis material images and $\mu_{1,2}(E_0)$ the attenuation coefficients of the basis materials at the photon energy E_0. The energy E_0 can be chosen according to the desired information: a lower E_0 results in a better soft tissue contrast; a higher E_0 produces a lower noise image.

2.5.2. Electron density images

The electron density is the basis of algorithms for precise dose calculation in radiation treatment planning. It can be extracted from the basis material images $a_{1,2}(x, y)$ by weighting them with the electron densities $\rho_{\mathrm{el},1,2}$ of the basis materials (Zhang *et al* 2018):

$$\rho_{\mathrm{el}}(x,\, y) = a_1(x,\, y)\cdot\rho_{\mathrm{el},1} + a_2(x,\, y)\cdot\rho_{\mathrm{el},2}. \tag{10}$$

2.5.3. Effective atomic number images

A heterogeneous material consists of a number of elements in different proportions. For the purposes of x-ray attenuation it can be described as a fictitious element with an effective atomic number Z_{eff} (Murty 1965). The effective atomic number for a material of known composition can be calculated by

$$Z_{\mathrm{eff}} = \sqrt[3]{\sum m_{1,2}\cdot Z_{1,2}^3}\,, \tag{11}$$

where $Z_{1,2}$ is the atomic number of the respective basis material and $w_{1,2}$ its fractional mass. The basis material images $a_{1,2}(x, y)$ allow the calculation of mass fraction images $m_{1,2}$:

$$m_{1,2}(x,\, y) = \frac{a_{1,2}(x,\, y)\cdot\rho_{1,2}}{a_1(x,\, y)\cdot\rho_1 + a_2(x,\, y)\cdot\rho_2} \tag{12}$$

with the mass densities $\rho_{1,2}$ of the basis materials. Thus, an effective atomic number image can be calculated with

$$Z_{\mathrm{eff}}(x,\, y) = \sqrt[3]{m_1(x,\, y)\cdot Z_1^3 + m_2(x,\, y)\cdot Z_2^3}\,, \tag{13}$$

where $Z_{1,2}$ are the atomic numbers of the basis materials.

2.6. Material phantom and *ex-vivo* measurements

2.6.1. Material phantom

In conventional images, different materials can look very similar. We measured a cylindrical material phantom to show the improvements for visual material differentiation and investigated the quantitative accuracy of our dual energy method. The cylindrical material phantom has a diameter of 3 cm and consists of a 3D printed cylinder made of polylactide (PLA) with different inserts. From bottom to top, the cylinder inserts are liquid water (H_2O), PVC, POM, aluminum (Al), graphite (C) and magnesium (Mg). On top, an artificial bone equivalent plastic cylinder (CIRS 062MA-07 from CIRS Inc., Norfolk, USA) is placed. It consists of an 800 mg cm^{-3} hydroxyapatite core (bone equivalent) and a water equivalent plastic surrounding. With the low energy spectrum (50 kV, 2.0 mA, 1 mm Al filter) and the high energy spectrum (100 kV, 0.2 mA, 1 mm Al filter), two CT images of the phantom were acquired, each with 720 different angles and a total dose of 15.8 cGy. The obtained CT images were decomposed into POM and PVC basis material images. Then, the basis material images were used to calculate VMIs (equation (9)), an electron density image (equation (10)) and an effective atomic number image (equation (13)). In principle, VMIs as well as the electron density and effective atomic number images are suitable for quantitative analysis. Due to the manufacturing process, the exact compositions for POM and PVC, especially the chlorine content in PVC, can vary. This affects the attenuation coefficient and we cannot work with the actual, but only with nominal values. Thus, the quantitative analysis of the VMI is not meaningful at this point. Since the electron density and the effective atomic number are less affected, a quantitative evaluation of the method can be done with these two quantities.

2.6.2. Ex-vivo *mouse measurements*

As the SARRP is mainly used for irradiation of mice, the presented method was also evaluated with an *ex-vivo* mouse measurement. The advantage of dual energy imaging in a mouse is best demonstrated with bones and iodine contrast agent.

For the dose calculation, one of five materials (air, lung, muscle, fat, bone) has to be assigned to each voxel in the CT image in the SARRP treatment planning system. Without dual energy images, bones and iodine can hardly be distinguished and the dose calculation algorithm for treatment planning would count iodine absorbing organs as bones. As the contrast agent is metabolized during the time needed for treatment planning, wrong dose distributions would be calculated. Therefore, the examiner at the SARRP has to correct the values of the iodine absorbing organs by hand. Due to the K-edge of iodine at 33 keV, the equations from section 2.1 cannot be solved properly with a POM and PVC basis. The quantitative values for iodine are therefore not correct. Nevertheless, our dual energy images provide additional qualitative information and can help to identify areas with iodine, extract them and substitute the iodine value automatically with a nominal soft-tissue value.

We measured a dead mouse, which was placed in formalin. In a small capsule, an iodine solution was prepared with water and the x-ray contrast agent Imeron 300 mg ml^{-1} (Bracco Imaging GmbH, Konstanz, Germany). The iodine concentration is chosen like it would be in the blood of a living mouse during a CT (about

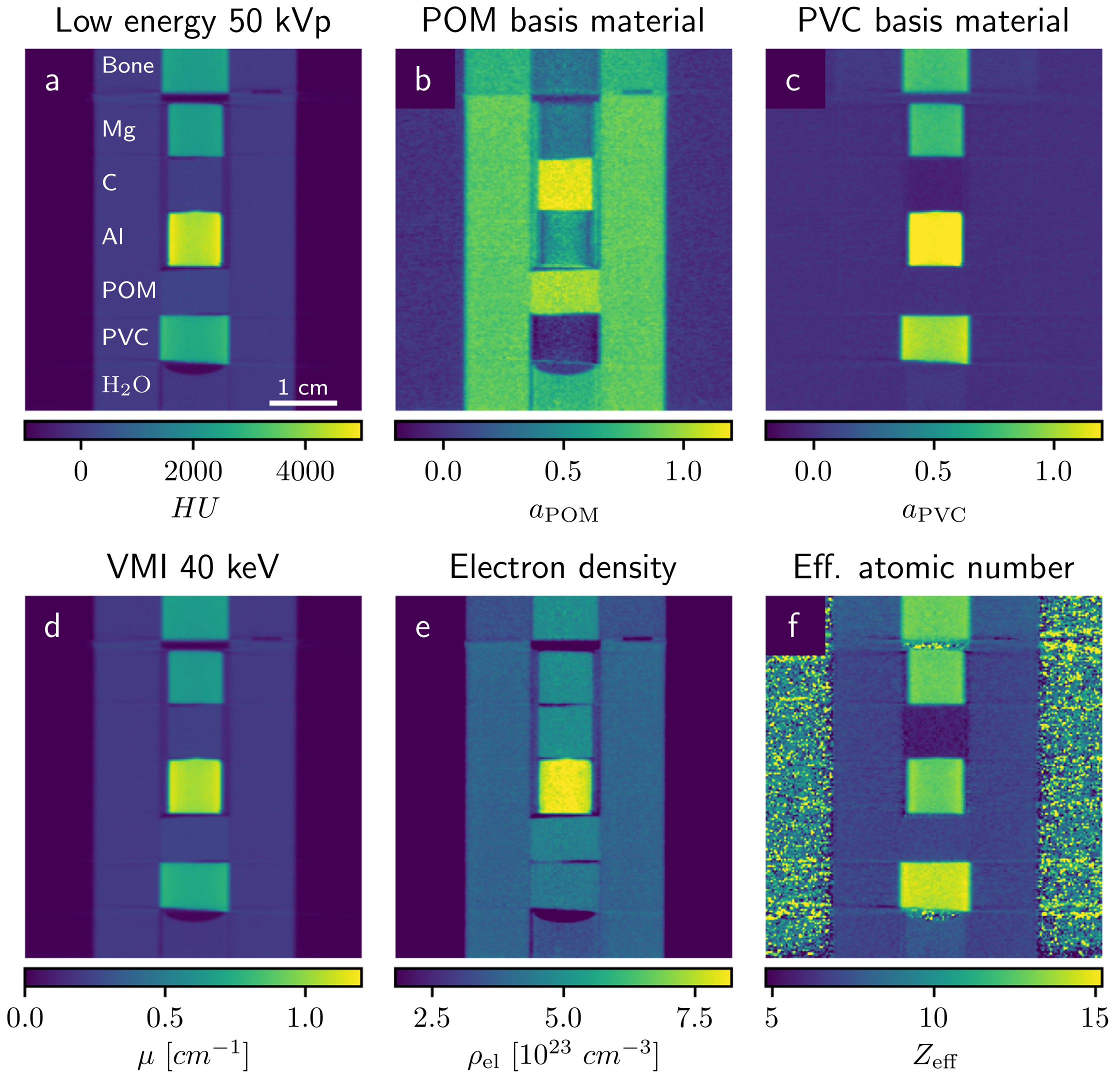

Figure 6. Dual energy images of a material phantom. In contrast to the polychromatic CT image (a), the basis material images of POM (b) and PVC (c) allow a better differentiation of the materials. The virtual monochromatic image at 40 keV (d), the electron density image (e) and the effective atomic number image (f) are calculated from the basis material images.

15 mg ml^{-1}). The iodine capsule is placed near the body between the front paws of the mouse. The mouse was scanned on a holder of PLA and a small material phantom with POM, PVC, and water was placed on top to verify the correct material decomposition. The low energy spectrum is the same as above (50 kV, 2.0 mA and 1 mm Al filter). For the high energy spectra the tube current was reduced (100 kV, 0.1 mA, 1 mm Al filter). For each CT, 1440 projections were recorded. Afterwards, the obtained raw data sets were decomposed into basis material images of POM and PVC, and the electron density and a VMI at 100 keV was calculated.

3. Results

3.1. Material phantom measurements

The low energy image (50 kVp) and the calculated DECT images are shown in figure 6. The two basis material images show more noise than the low energy images, but yield an improved visual differentiation of the materials. For instance, while magnesium and PVC look very similar without further windowing in the low energy image 50 keV, a clear distinction is possible in the POM image.

For the quantitative analysis, the mean values in an area of 10x10 pixels in the center of the cylinder along the cylinder axis are plotted (figure 7). Theoretical values from NIST (Hubbell and Seltzer 1995), ICRU Report 44 (White *et al* 2016), and the manufacturer specification on the bone density plug were used for comparison.

For the electron densities the relative deviations are all below 5%. The mean error is 2.6%. The value of bone is of particular interest, because the electron density is precisely known. Apart from the calibration materials POM (+0.1%) and PVC (−0.9%), the best value can be achieved here with an error of +2.3%.

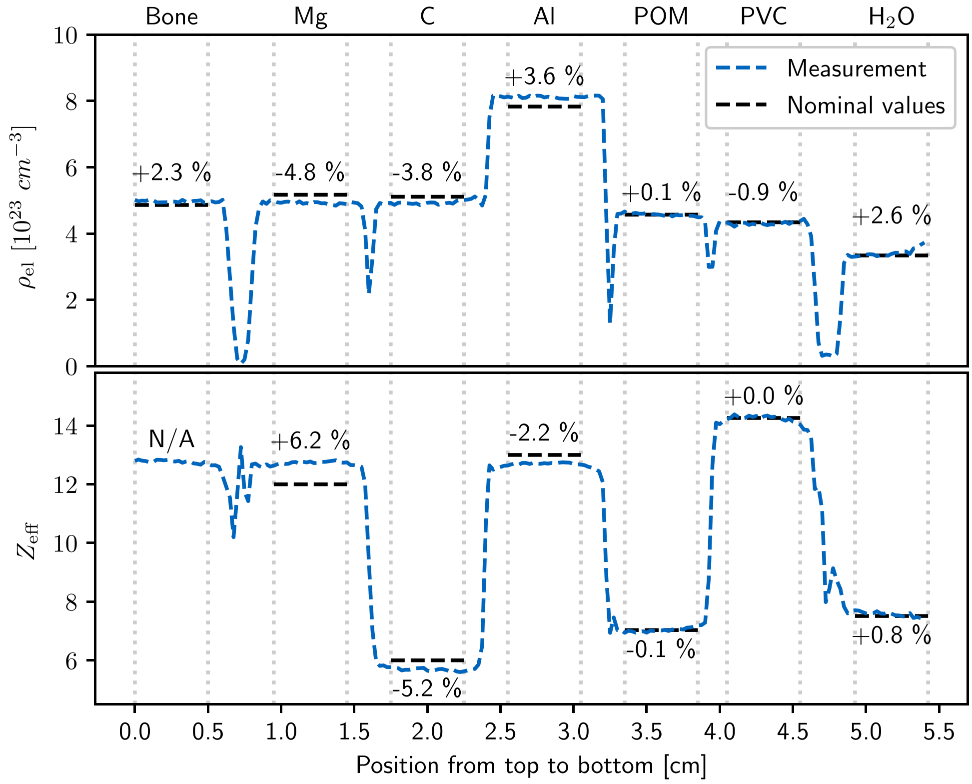

Figure 7. Electron density and effective atomic number accuracy. The electron density and the effective atomic number calculated from the basis material images are compared with the theoretical values for the different materials. The average values in an area of 10 × 10 pixels in the center of the cylinder are plotted along the cylinder axis. The relative deviations from the theoretical values are significantly below 10% for all materials. The nominal values were taken from NIST (Hubbell and Seltzer 1995), ICRU Report 44 (White *et al* 2016) and the manufacturer specification on the bone density plug.

For the effective atomic number the mean error is 2.4%, but the single materials show slightly higher relative deviations up to 6.2%. For both, electron density and atomic number, the highest errors occur for magnesium and graphite.

3.2. *Ex-vivo* mouse measurements

The dual energy images of the mouse are shown in figure 8. In the polychromatic images, bone and the iodine capsule show very similar HU values. In the POM basis image, the most significant difference is found as bone appears dark and iodine is the lightest of all tissue types. The PVC image does not contribute significantly to a better differentiation. Since the electron density image and the VMI are calculated from the basis material images, they both provide a noticeable difference between bone and iodine.

For iodine-corrected images, the different dual energy images are processed with thresholding to extract the iodine. In a first step, a threshold is applied to the low/high energy images to get only the bones and regions with iodine uptake. To distinguish between bone and iodine, another threshold is applied to the material decomposed images resulting in a map of high iodine uptake regions. All included pixels are set to a nominal tissue value. The benefit of the resulting iodine corrected images is a correct segmentation.

Regions with iodine can be extracted well without further segmentation methods. At the transition between regions with and without iodine, a few pixels remain assigned incorrectly. These can either be assigned manually in the treatment planning software or neglected. Since small residues of the contrast agent are usually still to be found in these regions, the real situation is consistent with a few uncorrected pixels in the iodine corrected images.

4. Discussion

For dual energy imaging at the SARRP a dual energy calibration was established. The originally proposed EDEC (Stenner *et al* 2007) does not work on the SARRP without adaptation because the SARRP internally scales the values of its projections and reconstructed images in an unknown way. In addition, the SARRP geometry makes it difficult to select appropriate dimensions for the calibration cylinders. The workaround with an artificial CT

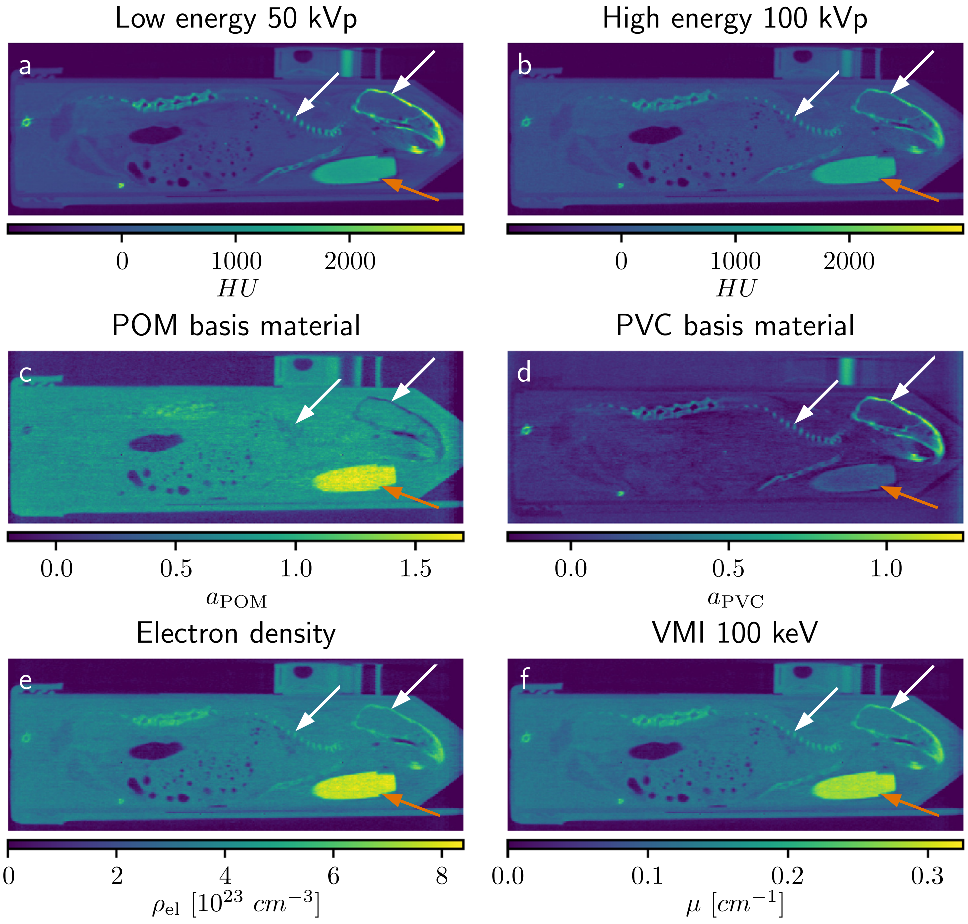

Figure 8. Dual energy images of an *ex-vivo* mouse with an Iodine capsule. The polychromatic CT images are acquired with the low (a) and the high energy (b) spectrum. The decomposed basis material images of POM (c) and PVC (d) are used to calculate the electron density image (e) and the virtual monochromatic image at 100 keV (f). The dual energy images allow a better differentiation of the capsule with iodine solution (orange arrow) from the bone structures (white arrows) than the polychromatic images.

image with values from a real measurement not only enables the use of a simple calibration but also allows us to choose the size of the calibration phantom to our needs.

It should be mentioned that the size of the calibration phantom in the artificial image has an influence on the material decomposition. The coefficient vector entries change significantly by changing the cylinder size. In simulations, it could be shown that the diameters of POM and PVC in the artificial CT images should cover at least the longest path length through the actual sample in the CT images. Figure 9 shows the influence of the calibration size on the material decomposition for measurements on phantoms of different sizes. The calibration was performed with 40 mm POM and 10 mm PVC. Different combinations of POM and PVC cylinders were used for the measurement, some smaller than the calibration phantom and some larger than the calibration phantom. In the present figure, only the POM material image is shown, which is calculated during the material decomposition. If the measured phantom is smaller than or equal to the calibration phantom, an accurate material decomposition is possible. The larger the measured phantom then becomes, the more artifacts can be observed in the material decomposition. In summary, calibrations with an oversized calibration phantom can decompose smaller samples of material effortlessly, whereas strong artifacts occur with undersized calibration cylinders. For very high absorbing materials like titanium, other calibration materials with a higher attenuation coefficient should be chosen.

Our SARRP shows very stable HU values over several months in quality assurance measurements, and we assume that the calibration remains equally stable. It is therefore not necessary to perform a calibration before each measurement. To ensure that the calibration and the material decomposition are still correct, two small cylinders of POM and PVC (diameter of 1 cm), are measured with our samples. With their values in the material images, the stability can be verified.

We are aware that by converting the measured CT images into sinograms, additional artifacts could be induced compared to working with the actual projections. Nevertheless we take this approach because we still want to reconstruct with the reconstruction software of the SARRP, which cannot deal with the calculated basis

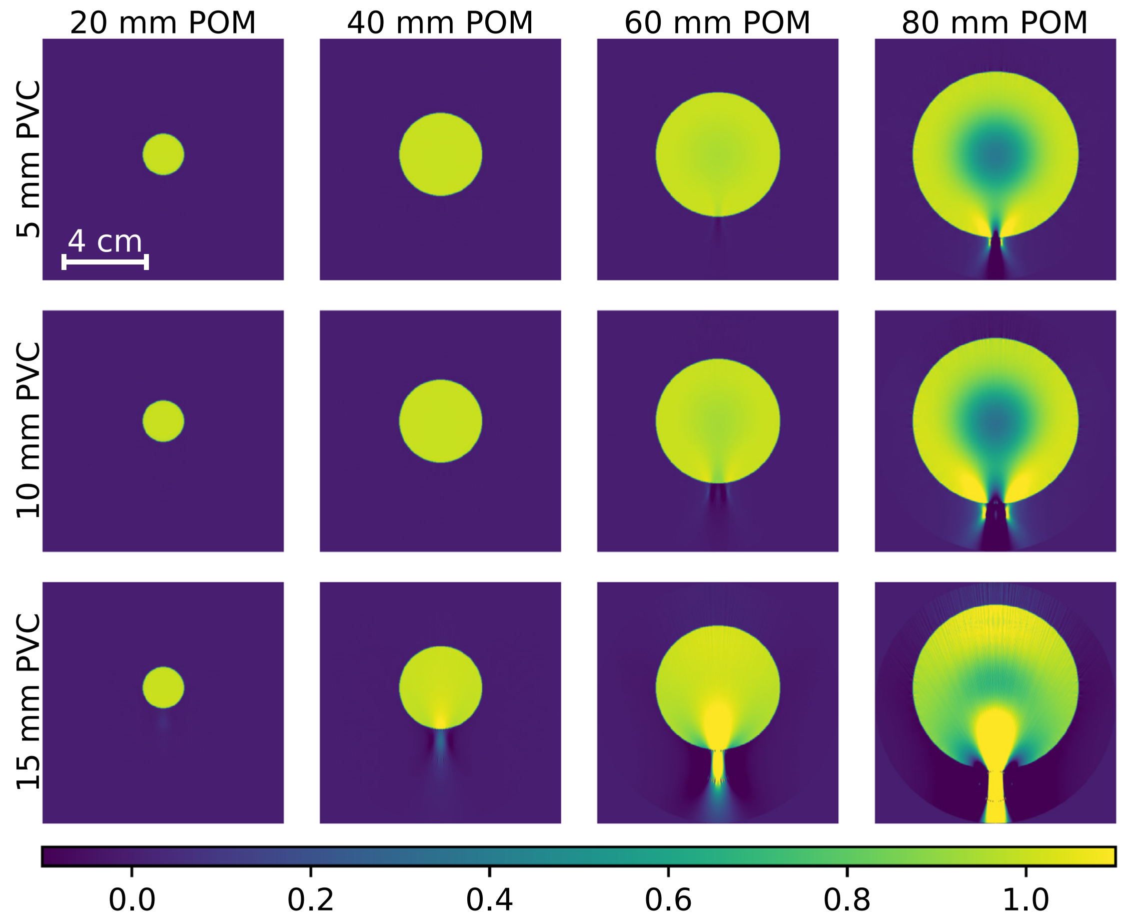

Figure 9. Effect on the material decomposition for a too small/too large calibration phantom. A calibration was performed with 40 mm POM and 10 mm PVC. For the measurement, differently sized POM and PVC cylinders were placed side by side. The sizes are given by the column and row labels respectively. The POM basis material images show an accurate material decomposition for measurement samples smaller than or equal to the calibration phantom size, but more and more artifacts occur for bigger measurement sample sizes.

material projections properly. However, our method is basically able to directly compute the measured projections instead of sinograms when using a custom reconstruction software. In this case, it must be noted that the SARRP acquires the projections from slightly different angles for each measurement. If the projection angles of the two DECT data sets differ too much, the respective images should be excluded from the reconstruction.

The dual energy images of the material phantom show more noise in the basis material images than the conventional image. This could be due to the forward and back projection and also the algorithm itself. As both images are used for the VMI, the electron density image and the effective atomic number image, the noise cancels out and the images look more homogeneous. In the effective atomic number image, air looks quite irregular. As both basis material images have a value around zero for air, the denominator of equation (12) is almost zero and the values for the fractional mass in air are not reliable. To avoid the distraction of the user, air values can be set to zero. In the presented method, the electron density image and the effective atomic number image are calculated from the basis material images using the equations (10) and (13). The accuracy of ρ_{el} and Z_{eff} therefore depends strongly on the exact knowledge of the electron density and effective atomic number of the basis materials. Although we only used nominal values in the present work, we achieved mean relative errors of the electron density and the effective atomic number of 2.6% for ρ_{el} and 2.4% for Z_{eff}, respectively. A previously published paper investigated the electron density and the effective atomic number of a material phantom using different low energy and high energy spectra combinations with a total dose of 86 cGy (Vaniqui *et al* 2018). There, relative errors of 0.8% for ρ_{el} and 1.6% for Z_{eff} could be reached, though applying a completely different approach with fitting curves (Saito 2012, Landry *et al* 2013). The accuracy of our method could be improved by using other basis materials like tissue equivalent plastic with exactly known electron density and effective atomic number. However, our errors are considered acceptable for our purposes.

When implementing DECT at the SARRP, the dose has to be considered. In particular, the dose of conventional imaging should not be exceeded. To achieve this, the number of projection angles is changed compared to conventional imaging. For our results, we decreased the number of angles equally for both spectra to decrease the dose. Our ongoing research shows that the number of projections can also be different for the two spectra. If the number of projections is further reduced for the low energy spectrum, the remaining dose can be used for more projections with the high energy spectrum. Depending on the application, this might be interesting for the user if very small structures are to be resolved.

The dual energy images of the mouse can help the examiner to identify iodine. The right choice of the spectra is essential for the differentiation of bone and iodine. Especially the POM basis image and the electron density allow an extraction of iodine using thresholds. The resulting correct segmentation contributes strongly to a correct dose calculation.

5. Conclusions

In this work, we have demonstrated that dual energy imaging is feasible at a Small Animal Radiation Research Platform (SARRP) without changes in the setup. Because of the SARRP geometry and reconstruction algorithm, dual energy imaging is done by using the Empirical Dual Energy Calibration algorithm with an artifical CT image based on measured values. After calibration, material decomposed basis material images, virtual monochromatic images, an electron density image and an effective atomic number image can be calculated from two sequentially acquired CTs. With these dual energy images, the differentiation of materials could be improved, which was explicitly shown with bone and iodine contrast agent in an *ex-vivo* mouse. The quantitative evaluation of the method with a material phantom yielded a good agreement with the theoretical values. It could be demonstrated that the segmentation and therefore the treatment planning process on a SARRP can be improved with our method.

Acknowledgments

This work was funded by the German Research Foundation (DFG) within the research training group GRK 2274.

ORCID iDs

Manuela Anna Duda https://orcid.org/0000-0002-7148-0828
Andreas Grad https://orcid.org/0000-0001-5501-5654
Severin Kampfer https://orcid.org/0000-0002-9521-1809
Sophie Dobiasch https://orcid.org/0000-0001-5358-7237
Stephanie Elisabeth Combs https://orcid.org/0000-0002-5233-1536
Jan Jakob Wilkens https://orcid.org/0000-0002-1851-0581

References

Agostini A, Borgheresi A, Mari A, Floridi C, Bruno F, Carotti M, Schicchi N, Barile A, Maggi S and Giovagnoni A 2019 Dual-energy CT: theoretical principles and clinical applications *Radiol Med* **124**

Alvarez R and Macovski A 1976 Energy-selective reconstructions in X-Ray computerized tomography *Phys. Med. Biol.* **21** 733–44

Bazalova-Carter M, Carrier J F, Beaulieu L and Verhaegen F 2008 Dual-energy CT-based material extraction for tissue segmentation in Monte Carlo dose calculations *Phys. Med. Biol.* **53** 2439–56

Boone J and Seibert J 1997 An accurate method for computer-generating tungsten anode x-ray spectra from 30 to 140 kV *Med. Phys.* **24** 1661–70

Cardinal HN and Fenster A 1990 An accurate method for direct dual-energy calibration and decomposition *Med. Phys.* **17** 327–41

Dobiasch S, Kampfer S, Burkhardt R, Schilling D, Schmid T E, Wilkens J J and Combs S E 2017 BioXmark for high-precision radiotherapy in an orthotopic pancreatic tumor mouse model: Experiences with a liquid fiducial marker *Strahlenther Onkol.* **193** 1039–47

Hubbell J H and Seltzer S M 1995 Tables of X-Ray mass attenuation coefficients and mass energy-absorption coefficients from 1 keV to 20 MeV for elements Z = 1 to 92 and 48 additional substances of dosimetric interest *NIST Interagency Rep.* NISTIR 5632 (https://doi.org/10.18434/T4D01F)

Kappadath S and Shaw C 2003 Dual-energy digital mammography: Calibration and inverse-mapping techniques to estimate calcification thickness and glandular-tissue ratio *Med. Phys.* **30** 1110–7

Kharfi F 2012 Mathematics and physics of Computed Tomography (CT): demonstrations and practical examples *Imaging and Radioanalytical Techniques in Interdisciplinary Research* (London: IntechOpen) (https://doi.org/10.5772/52351)

Landry G, Seco J, Gaudreault M and Verhaegen F 2013 Deriving effective atomic numbers from dect based on a parameterization of the ratio of high and low linear attenuation coefficients *Phys. Med. Biol.* **58** 6851–66

Murty R 1965 Effective atomic numbers of heterogeneous materials *Nature* **207** 398–9

Saito M 2012 Potential of Dual-Energy subtraction for converting CT numbers to electron density based on a single linear relationship *Med. Phys.* **39** 2021–30

Schyns L, Almeida I S, Hoof S J, Descamps B, Vanhove C, Landry G, Granton P V and Verhaegen F 2016 Optimizing dual energy cone beam CT protocols for preclinical imaging and radiation research *Br. J. Radiol.* **90** 20160480

Sellerer T, Ehn S, Mechlem K, Duda M, Epple M, Noël P B and Pfeiffer F 2019 Quantitative dual-energy micro-CT with a photon-counting detector for material science and non-destructive testing *PLoS ONE* **14** e0219659

Sellerer T *et al* 2018 Dual-energy CT: a phantom comparison of different platforms for abdominal imaging *Eur. Radiol.* **28** 2745–55

Stenner P, Berkus T and Kachelriess M 2007 Empirical dual energy calibration (EDEC) for cone-beam computed tomography *Med. Phys.* **34** 3630–41

Vaniqui A, Schyns L, Almeida I, Van der Heyden B, Hoof S and Verhaegen F 2017 The impact of dual Energy CT imaging on dose calculations for pre-clinical studies *Radiat. Oncol.* **12**

Vaniqui A, Schyns L, Almeida I, Van der Heyden B and Verhaegen F 2018 The effect of different image reconstruction techniques on pre-clinical quantitative imaging and dual-energy CT *Br. J. Radiol.* **92** 20180447

Verhaegen F, Granton P and Tryggestad E 2011 Small animal radiotherapy research platforms *Phys. Med. Biol.* **56** R55–83

White D, Booz J, Griffith R, Spokas J and Wilson I 2016 ICRU Report 44 *J. Int. Commission Radiat. Units Meas.* (https://doi.org/10.1093/jicru/os23.1.Report44)

Wong J *et al* 2008 High-Resolution, small animal radiation research platform with x-ray tomographic guidance capabilities *Int. J. Radiat. Oncol., Biol., Phys.* **71** 1591–9

Zhang S, Han D, Politte D, Williamson J and O'Sullivan J 2018 Impact of joint statistical dual-energy CT reconstruction of proton stopping power images: Comparison to image- and sinogram-domain material decomposition approaches *Med. Phys.* **45** 2129–42